Westward Generation of Eastward-Moving Tropical Convective Bands in TOGA COARE

SHOICHI SHIGE* AND TAKEHIKO SATOMURA

Graduate School of Science, Kyoto University, Kyoto, Japan

(Manuscript received 5 July 2000, in final form 15 June 2001)

ABSTRACT

Mechanisms responsible for westward generation of eastward-moving tropical convective bands in the Tropical Ocean and Global Atmosphere Coupled Ocean–Atmosphere Response Experiment (TOGA COARE) are investigated using a two-dimensional numerical cloud model. Sequential generation of new convective bands to the west of an old eastward-moving convective band is successfully simulated in an environment of a convectively active day during TOGA COARE, characterized by west winds at low levels and strong easterlies aloft.

It is concluded that the westward generation of new convective bands is explained by a gravity wave mechanism. Two westward-propagating modes excited below the convective cells moving westward relative to the convective bands appear to play an important role. A slow-propagating mode ($\sim$15 m s^{-1}) excited by a shallow convective band is ducted in the troposphere under an unstable layer of small Richardson number containing its critical level. A fast-propagating mode ($\sim$25 m s^{-1}) excited by a deep convective band is ducted in the troposphere under the remaining region of the convective cell containing its critical level. These two modes propagate horizontally to the west and promote the growth of shallow convection into long-lived convective bands. A dry model with thermal forcing representing the convective cell showed that preferential excitation of westward-propagating waves below the convective cell is due to westward motion and ascension of the convective cell. A comparative simulation without the critical level confirms the proposed gravity wave mechanism.

1. Introduction

A hierarchy of tropical convective activity over the equatorial western Pacific has been investigated by many researchers. Nakazawa (1988) found that ''super cloud clusters'' (SCC) move eastward with a phase speed of about 10–15 m s^{-1}, and disturbances propagate westward with a lifetime of $\sim$2 days within a super cloud cluster during the active phase of intraseasonal oscillation (ISO; Madden and Julian 1971), using the 3-hourly satellite infrared data. Takayabu (1994) reported the dominance of a quasi-2-day mode in the cloud field in the December–February season, and identified this mode with the westward-propagating $n = 1$ inertio–gravity wave theoretically found by Matsuno (1966).

Although Matsuno (1966) found an eastward-propagating $n = 1$ inertio–gravity wave as well as a westward-propagating $n = 1$ inertio–gravity wave as linear solutions under the equatorial beta plane approximation, an eastward-propagating $n = 1$ inertio–gravity wave has never been observed.[1] Yoshizaki (1991) analytically studied linear responses to localized heating, which moves westward or eastward uniformly on the equatorial beta plane. He showed that the westward-propagating inertio–gravity wave is strongly excited by the westward-moving heating, while the eastward-propagating wave is not so excited by the eastward-moving heating. He pointed out that this arises from the difference in meridional structure. His results indicated the possible dominance of the westward-propagating inertio–gravity wave when the clouds are organized and propagate westward on the equator.

One might infer that mesoscale convective bands propagate westward owing to easterly trade winds; thus, they act as the westward-moving heating that excites the westward-propagating inertio–gravity wave. Lin and Johnson (1996), however, reported that the typical zonal wind in the convectively active phase of the ISO was westerly through the lower troposphere during the Tropical Ocean Global Atmosphere Coupled Ocean–Atmosphere Response Experiment (TOGA COARE; Webster and Lukas 1992). LeMone et al. (1998) demonstrated

* Current affiliation: Earth Observation Research Center, National Space Development Agency of Japan, Tokyo, Japan.

Corresponding author address: Dr. Shoichi Shige, Earth Observation Research Center, National Space Development Agency of Japan, Harumi Island Triton Square, Office Tower X, 1-8-10 Harumi, Chuo-ku, Tokyo, 104-6023, Japan.
E-mail: shige@eorc.nasda.go.jp

[1] In the equatorial lower stratosphere, the disturbances that likely correspond to eastward-propagating $n = 1$ inertio–gravity waves were observed by Wada et al. (1999).

that, consistent with this, 80% of the convective bands sampled by the aircraft in TOGA COARE propagate toward the east. Shipboard radar observations (Rickenbach and Rutledge 1998) also suggested that most mesoscale convective systems moved eastward with low-level westerlies. Hence it is difficult for COARE convective bands to act as the westward-moving heating that excites the observed westward-propagating inertio–gravity waves.

Some case studies reported generation of a new convective band to the west of an old convective band in TOGA COARE. Mori (1995) observed sequential generation of a new convective band to the west of an old convective band on 10–12 November during TOGA COARE. Lewis et al. (1998) also reported generation of a new convective band to the west of an old convective band on 20 February 1993. Halverson et al. (1999) examined a convectively active day, 11 February 1993, in which several convective bands evolved and moved eastward across the TOGA COARE Intensive Flux Array (IFA) under westerly wind burst conditions. They reported that a convective band moved eastward and a new band formed to its west, with zonal separation between individual bands of 150–200 km. The westward generation of new convective bands observed by Mori (1995), Lewis et al. (1998), and Halverson et al. (1999) occurred in a group of cloud clusters, which is a part of the 2-day westward-propagating disturbance. Westward generation of new convective bands possibly acts as the westward-moving heating that excites the westward-propagating inertio–gravity waves. Thus, westward generation of new convective bands is not just an interesting phenomena—it is also expected to play an important role in the interaction between mesoscale convective systems and the 2-day westward-propagating disturbances.

Recently, researchers have focused on the role of high-frequency tropospheric gravity waves in the hierarchy of tropical convective activity. Oouchi (1999) simulated SCC-like hierarchical cloud organization under easterlies at low levels, using a two-dimensional model. He demonstrated that high-frequency tropospheric gravity waves play the following key role in the successive formation of cloud clusters to the east. Inner convective systems of SCC move westward owing to easterlies at low levels. Gravity waves excited by these convective systems propagate eastward, and contribute to the formation of new clouds to the east where the low-level atmosphere is moistened by the wind-induced surface heat and moisture exchange (WISHE; Emanuel 1987; Neelin et al. 1987). Lin and Johnson (1996), however, reported that observations during TOGA COARE do not appear to support the WISHE mechanism. Furthermore, the question of why gravity waves propagating opposite to the direction of the motion of the storm are preferentially excited by inner convective systems of SCC was not answered.

Recent studies have investigated gravity waves generated by prescribed heating sources resembling a mesoscale convective system (Nicholls et al. 1991; Mapes 1993; Pandya et al. 1993; Pandya and Durran 1996; McAnelly et al. 1997). Pandya and Durran (1996) demonstrated that gravity waves forced by the low-frequency component of the latent heating and cooling in the leading edge determined the mesoscale circulation around squall lines; the mesoscale circulation includes an ascending front-to-rear flow, a midlevel rear inflow, and a mesoscale up- and downdraft in the trailing stratiform region. Pandya and Durran (1996) attributed the preferential rearward excitation of low-frequency tropospheric gravity waves to the tilt of the forcing.

These low-frequency tropospheric gravity waves have little resemblance to monochromatic gravity waves, in the sense that they do not have a periodic structure in time or space, as pointed out by Mapes (1993). In contrast, high-frequency gravity waves are more nearly monochromatic. The mechanism for excitation of high-frequency gravity waves should therefore be different from that of low-frequency gravity waves. Fovell et al. (1992), using a two-dimensional numerical model, demonstrated that the high-frequency stratospheric gravity waves propagating upward and opposite to the direction of the motion of the storm are preferentially excited by a mesoscale convective storm. Their simulations showed that the most important factor for the preferential generation of gravity waves was not the tilt of the forcing, but the presence or absence of horizontal propagation in the forcing.

In addition to wave generation mechanisms, wave propagation characteristics are different. The direction of energy propagation for gravity waves in a resting atmosphere can be described by

$$\cot(\alpha) = \frac{\omega}{\sqrt{N^2 - \omega^2}} \tag{1}$$

(Pandya et al. 2000), where α is the angle of energy propagation measured from the vertical, N is the Brunt–Väisälä frequency, and ω is the frequency of the wave. Equation (1) predicts that the low-frequency gravity waves can propagate for long distances while retaining significant energy and would be expected to influence tropospheric circulations. Equation (1) also predicts that the high-frequency gravity waves would normally lose their energy through vertical propagation into the middle atmosphere. A mechanism for trapping wave energy in the troposphere is therefore necessary for them to play a role in the westward generation of new convective bands.

Shige (1999) detected mesoscale disturbances in the equatorial western Pacific lower troposphere having periods of 1–2 h in data from wind profilers with fine time resolution during TOGA COARE. He estimated a disturbance having a 60-min period and a 6-h duration as a gravity wave. He concluded that this gravity wave was excited by a mesoscale cloud line and then propagated

westward in a wave duct in the troposphere under strong easterlies aloft, caused by the mechanism proposed by Lindzen and Tung (1976). The strong easterlies aloft are common to the westward regeneration convective activity cases (see Fig. 2 of Mori 1995; Figs. 5 and 6 of Lewis et al. 1998; Fig. 10 of Halverson et al. 1999), and they are expected to play an important role for the wave duct.

The role of upper-level wind shear in the organization of mesoscale convective systems has received less attention than those of low- and midlevel wind shear. Barnes and Sieckman (1984) described two classes of tropical cloud convective lines over the tropical Atlantic in the GATE,[2] so-called fast- and slow-moving lines. Fast-moving lines developed with strong low-level shear and were nearly normal to the low-level shear, while slow-moving lines developed with weak low-level shear and were parallel to the shear from ~900 to 500 mb. Similar behavior was reported for tropical cloud convective lines in EMEX[3] by Alexander and Young (1992) and in TOGA COARE by LeMone et al. (1998), but with slow-moving lines parallel to the midlevel shear from 800 to 400 mb. Furthermore, LeMone et al. (1998) reported that with appreciable shear at low- and midlevels, the low-level shear determined the orientation of the primary convective band, while the midlevel shear determined whether trailing secondary bands would be present. Although the classification scheme of LeMone et al. (1998) allows for a more complex, yet still ordered, structure observed for convective systems than previous studies, this classification scheme does not account for the westward regeneration convective activity cases.

In the present study, we investigate mechanisms responsible for generation of a new convective band to the west of an old convective band, using a nonhydrostatic cloud model. We focus on the role of high-frequency tropospheric gravity waves generated by convective cells in the westward generation of new convective bands. The effect of the strong easterlies aloft on the westward generation of new convective bands is also examined.

2. Numerical model and initial conditions

a. Numerical model

The present study uses a nonhydrostatic cloud model, the Regional Atmospheric Modeling System (RAMS), developed at Colorado State University. The computation was carried out under a two-dimensional configuration. The Coriolis terms were neglected. The lower and upper boundary conditions were flat, rigid, and free-slip. The surface layer fluxes of heat and water vapor into the atmosphere were computed with the scheme of Louis (1979). Bulk moist processes, including the formation and interaction of clouds and precipitating liquid and ice hydrometers, were employed. The model domain was 950 km in the x direction (horizontal) and 27 km in the z direction (vertical). The horizontal resolution was 500 m. The vertical resolution was expanded from 50 m at the lower boundary to 500 m at the top of the domain; this varying vertical resolution was chosen to simulate a shallow cold pool near the lower boundary. A Rayleigh damping layer having a depth of 10 km was included at the top of the domain to reduce the reflection of gravity waves from the upper boundary. A radiation condition (Klemp and Wilhelmson 1978) was used for the lateral boundaries. The model domain was translated at a constant speed (13.84 m s^{-1}) to keep the simulated convective systems away from the lateral boundaries.

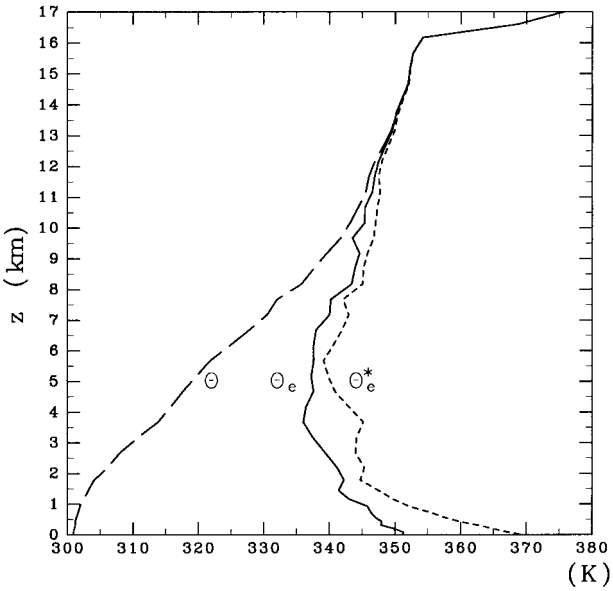

FIG. 1. Initial thermodynamic soundings used in model simulations, showing the vertical profiles of potential temperature θ (dashed line), equivalent potential temperature θ_e (solid line), and saturated equivalent potential temperature θ_e^* (dotted line).

b. Initial conditions

For all simulations discussed herein, the thermodynamic structure was specified according to the sounding of R/V *Vickers* at 0600 UTC 11 February 1993 (Fig. 1). The surface temperature was fixed at 302.15 K from the Integrated Sounding System (ISS) sea-surface temperature observation of R/V *Vickers* on 11 February 1993. It was the convectively active day during TOGA COARE examined by Halverson et al. (1999). They documented that nine convective bands evolved and moved from the direction of 255° (toward the east-northeast) across the region of shipboard radar in the TOGA

[2] GATE: (Global Atmospheric Research Program) Atlantic Tropical Experiment, conducted in the tropical Atlantic in 1974.

[3] EMEX: Equatorial Mesoscale Experiment, conducted north of Australia in 1987.

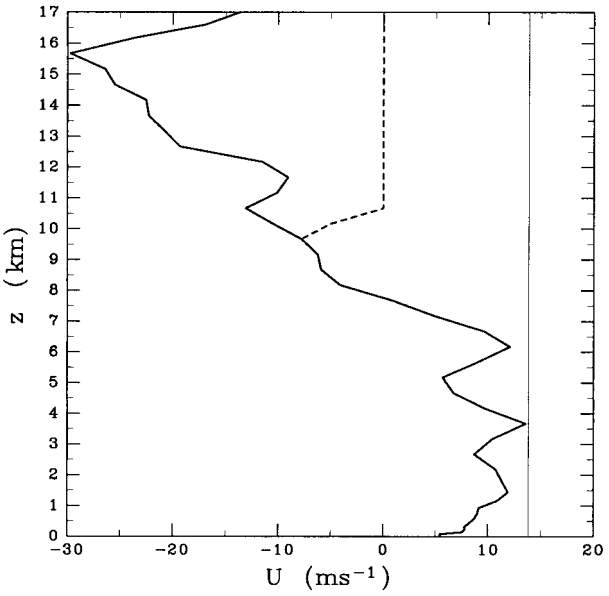

FIG. 2. Initial wind profiles for the CONTROL case (thick solid line) and NOEAST case (dotted line). The thin solid line indicates the translation speed of the model domain (13.84 m s^{-1}).

COARE IFA. These bands initiated from scattered convection in the western portion of the IFA, and with time they gradually intensified and grew to large convective bands before exiting the IFA to the east (see Fig. 4 of Halverson et al. 1999). The zonal separation between individual bands was characteristically on the order of 150 km.

We compared two simulations to examine the influence of upper tropospheric winds on the westward generation of new convective bands. The examined horizontal wind profiles are shown in Fig. 2. In the first case (CONTROL), the wind profile was specified according to the wind sounding in the storm motion direction of 75° of R/V *Vickers* at 0600 UTC 11 February 1993. Horizontal winds are westerlies at low to middle levels and easterlies aloft. Lin and Johnson (1996) reported that this is a typical profile in the convectively active phase of the ISO. In the other case (NOEAST), easterlies aloft are artificially reduced.

Convection was initiated by placing a warm thermal (a potential temperature excess of 4 K) having a horizontal width of 20 km and a vertical width of 3.2 km. This thermal was centered at 550 km from the left boundary (hereafter $x = 0$ km), and $z = 1.6$ km. The initial sounding used here was not moist enough to support the rate of development and strength of the observed convection. The above strong thermal was therefore used. It should be noted that the numerically simulated features did not vary qualitatively if the potential temperature excess is 2 K.

3. Results

A time-zonal cross section of the mixing ratio of rain at $z = 23.9$ m in the CONTROL case is shown in Fig. 3. The thin line in this figure indicates 0 m s^{-1} relative to the ground. The primary band near $x = 0$ km was initialized by the thermal bubble. Figure 3 clearly shows an asymmetry of precipitating clouds between the primary band's western and eastern sides. On the western side of the primary band, precipitating clouds became organized into long-lived bands B2 and B3. New bands sequentially developed to the west of old bands. Long-lived band B2 developed to the west of short-lived band B1, then long-lived band B3 developed to the west of band B2. In contrast, none of the small precipitating clouds become organized into long-lived bands on the eastern side.

The overall structures of the primary band's western and eastern sides are illustrated in Figs. 4a–c and 4d–f. These figures show vertical cross sections of the vertical velocity field superposed on the cloud outline. The cloud outline, defined as the region in which the mixing ratio of condensates exceeds 0.1 g kg^{-1}, is shown by a bold line. It is clear from Fig. 4 that there are differences in the horizontal scale and height of clouds between the western side and eastern side. The western side clearly exhibits sequential growth of shallow convection into deep convection to the west of old bands. At $t = 330$ min, the heights of short-lived band B1 and earlier B2 were about 10 km (Fig. 4a). Short-lived band B1 dissipated without growing into a large and deep convective system. After band B1 dissipated, band B2 became organized into a large, long-lived system, and its height reached about 14 km (Fig. 4b). After band B2 decayed in intensity, band B3 became organized into a large, long-lived system, and its height reached about 14 km (Fig. 4c). On the eastern side, however, small clouds were not organized on the mesoscale and their heights were less than 10 km (Figs. 4d–f).

Shipboard radar data collected during TOGA COARE provided evidence of abundant populations of midlevel *cumulus congestus* clouds in addition to the well-known large populations of shallow *cumulus* clouds, and deep *cumulonimbus* clouds in the tropics (DeMott and Rutledge 1998; Johnson et al. 1999). Although the cumulus congestus clouds with tops between 4.5 and 9.5 km do not produce heavy rain as the deep cumulonimbus clouds with tops near the tropopause, congestus are the most abundant of all precipitating clouds in TOGA COARE. Short-lived band B1, earlier B2, and earlier B3 on the western side, and all precipitating clouds on the eastern side can be classified into cumulus congestus clouds, while later B2 and later B3 can be classified as deep cumulonimbus counterparts. Johnson et al. (1999) pointed out that restriction of growth of congestus clouds to just above the 0°C level limits further enhancement of cloud buoyancy through glaciation.

We now focus on why cumulus congestus clouds can grow into deep, long-lived convective bands only on the western side. A possible explanation for the asymmetry of precipitating clouds between the western and eastern sides lies in the difference of surface thermo-

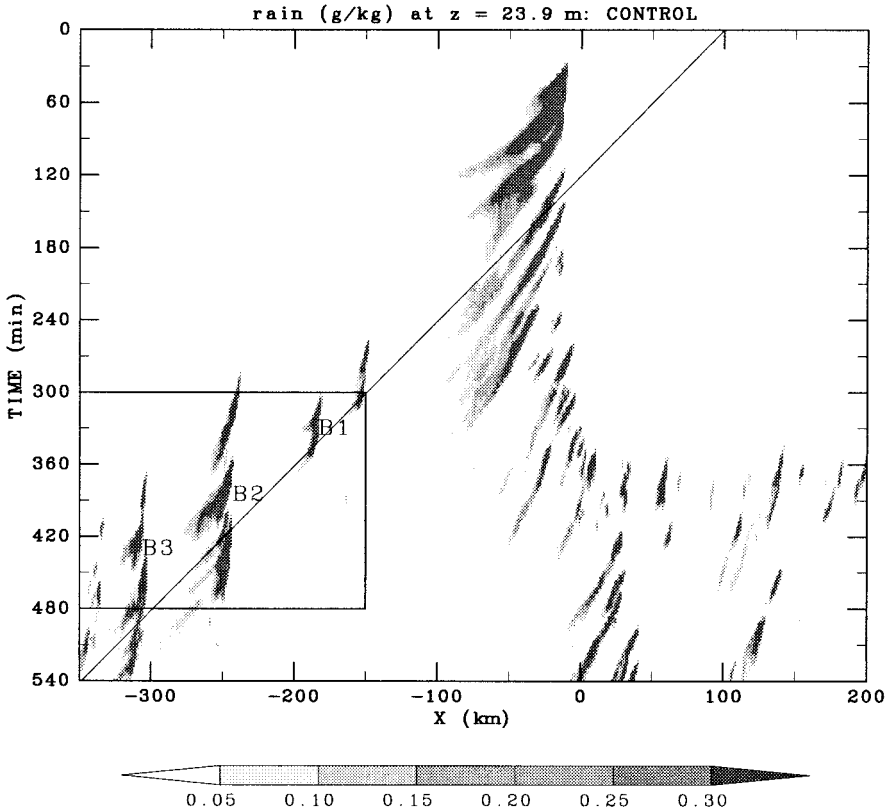

FIG. 3. Time-zonal cross section of mixing ratio of rain (g kg^{-1}) at $z = 23.9$ m in the CONTROL case. The degree of shading denotes the range of mixing ratio of rain, as indicated by the value bar at the bottom of the figure. The rectangle indicates the region that is expanded in Fig. 5. The thin line indicates 0 m s^{-1} relative to the ground. B1, B2, and B3 indicate precipitating bands.

dynamic conditions between the western and eastern sides due to an effect similar to WISHE (Emanuel 1987; Neelin et al. 1987). In order to examine the influence of the WISHE-like effect on the asymmetry of clouds between the western and eastern sides, we performed an additional simulation (NOWISHE). This simulation is the same as the CONTROL case except that the surface heat and moisture fluxes are calculated using a constant surface wind of 8.4 m s^{-1}, which is the averaged wind speed on the western side at $t = 240$ min in the CONTROL case. Precipitating clouds on the western side are still stronger than those on the eastern side as in the CONTROL case (not shown). Thus, the asymmetry of clouds between the western and eastern sides is not due to the WISHE-like effect.

An expanded view of the rectangle in Fig. 3 is illustrated in Fig. 5, which shows the time-zonal cross section of vertical velocity at $z = 6.675$ km and the mixing ratio of rain at $z = 23.9$ m. It is clear from Fig. 5 that the wave activity generated by the convective bands is biased to the western side. Disturbance D1 propagates westward from the band B1 and promotes the development of the band B2. Disturbance D3 then propagates westward from band B2 and promotes the development of band B3. Disturbance D1 has a horizontal wavelength $L_x = 12$ to 14 km and horizontal phase speed $c_x = -15$ to -16 m s^{-1} relative to the ground, while disturbance D3 has $L_x = 20$ to 21 km and $c_x = -24$ to -27 m s^{-1}. Additionally, disturbance D2 has a phase speed similar to that of disturbance D1, and disturbance D4 has a phase speed similar to that of disturbance D3, as shown in Fig. 5. These results suggest that slow-propagating waves (D1 and D2) are excited by shallower bands (B1 and earlier B2), and fast-propagating waves (D3 and D4) by deeper bands (later B2 and later B3). Once they have excited waves, these bands decay in intensity.

Figure 6 is the same as in Fig. 5 but for potential temperature and rain mixing ratio at $z = 23.9$ m in the CONTROL case. The cold pool spreading rearward from the primary band initialized by the thermal bubble is responsible for the initiation of band B1. Moncrieff and Liu (1999) showed that when the shear and surface flow vectors are in the same direction, lifting is generated in the upstream-propagating currents. This is the case here because the westerly shear at low levels and surface westerly can be seen in Fig. 2. However, the cold pool spreading rearward from the primary band was very shallow (about 500 m thick) and therefore, the speed was very slow. It should be noted that the western edge of the cold pool spreading from the primary band propagates eastward relative to the ground at a speed of 2 m s^{-1}. These characteristics of the simulated cold

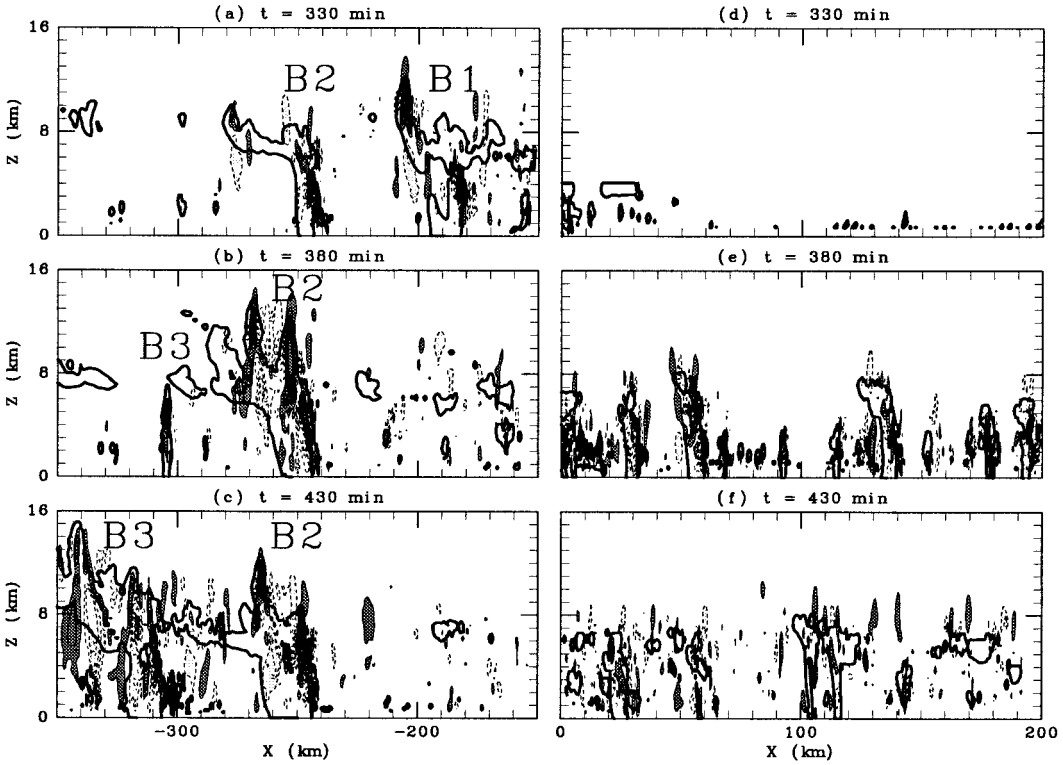

FIG. 4. Contours of vertical velocity (contour interval 1.0 m s^{-1}) and cloud outline (bold line) defined as the region in which the mixing ratio of condensates exceeds 0.1 g kg^{-1}; for (a)–(c) the western side and (d)–(f) the eastern side in the CONTROL case at $t = 330$, 380, and 430 min. Positive (negative) values are solid (dashed). Updrafts greater than 1.0 m s^{-1} are heavily shaded, and downdrafts less than -1.0 m s^{-1} are lightly shaded.

pool agree with the observation over the western Pacific ocean (Parsons et al. 1994). Thus, the cold pool spreading rearward from the primary band could not develop deep bands, or it does not account for westward generation speed of new convective bands. In fact, it is clear from Fig. 6 that the cold pool spreading rearward from the primary band is not responsible for the development of long-lived band B2. The initiations of convection are not always attributed to the cold pool, and differ from case to case. For example, disturbance D2 appears to contribute to the initiation of band B3 (Fig. 5).

The time sequence of westward-propagating disturbance D3 with a time interval of 6 min is illustrated in Fig. 7, which shows vertical cross sections of the vertical velocity field superposed on the cloud outline. Convective band B2 at $x = -240$ km propagated eastward by discrete growth of new convective cells at the leading edge of the gust front. An old convective cell denoted by ''C'' separated from the leading edge of band B2 at $x = -240$ km and moved westward relative to band B2, as shown in Figs. 7a,b. This behavior is typical of multicell storms and has been simulated by previous modeling studies (Rotunno et al. 1988; Fovell and Ogura 1988; Tao and Simpson 1989; Lafore and Moncrieff 1989; and many others). From model outputs at 2-min intervals (not shown), we see that cell C ascended with westward acceleration. Westward-propagating disturbance D3 of upward motion is produced below cell C.

Figure 8 shows the vertical velocity fields superimposed in potential temperature fields. The cold pool extends from the leading edge of the band B2 at $x = -240$ km to $x = -280$ km and does not pass under the shallow convection at $x = -305$ km (Fig. 8f). Thus, the cold pool of band B2 does not promote the growth of shallow convection into a long-lived convective band B3 at $x = -305$ km, as mentioned earlier. Cell C dissipates near $z = 14.5$ km until $t = 390$ min (Fig. 8c), since its closed contour region of high potential temperature has disappeared. The level where cell C dissipated roughly corresponds to the equilibrium level where the equivalent potential temperature of the parcel ascending from the surface crosses the environmental potential temperature (Fig. 1). The contours of potential temperature in Figs. 8c–e clearly show that the unstable region denoted by R remains after cell C has dissipated. Remaining region R moves near $z = 14.5$ km with a speed of about -21 m s^{-1} relative to the ground. Since this speed roughly corresponds to the mean horizontal wind near $z = 14.5$ km, remaining region R is considered to be passively advected by the mean horizontal wind. Even though cell C has dissipated, disturbance D3 propagates

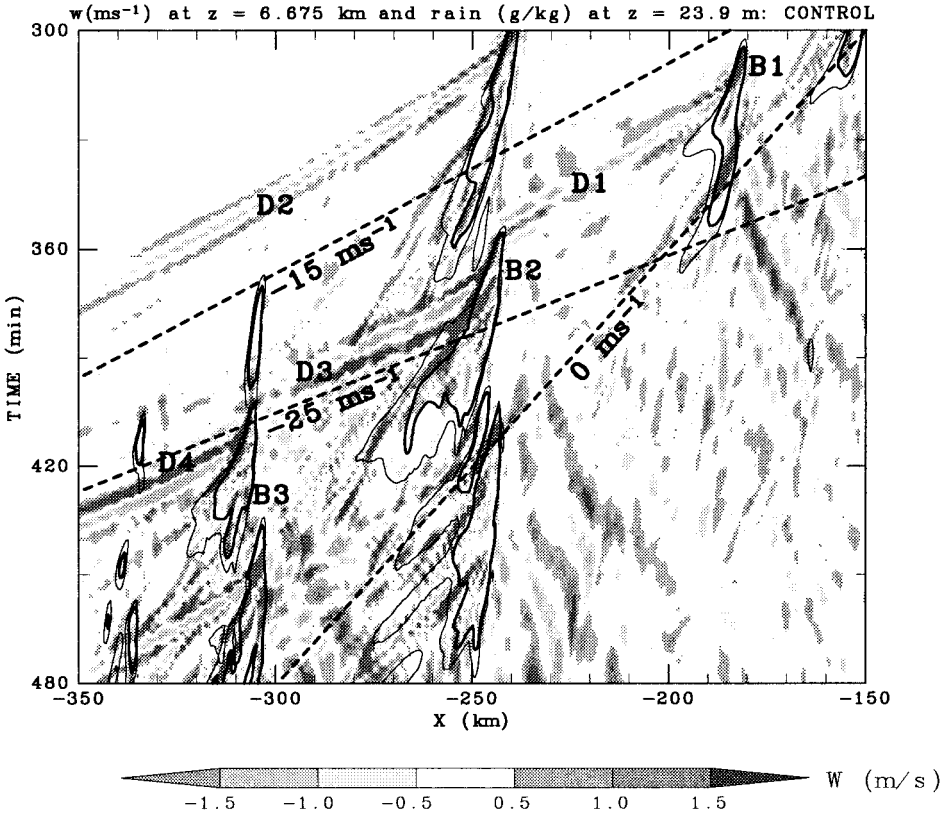

FIG. 5. Time-zonal cross section of vertical velocity (m s^{-1}) at $z = 6.675$ km and rain mixing ratio (g kg^{-1}) at $z = 23.9$ m in the CONTROL case illustrating an expanded view of the rectangle in Fig. 3. The degree of shading denotes the range of vertical velocities, as indicated by the value bar at the bottom of the figure. The heavy (light) solid lines indicate the region in which the rain mixing ratio exceeds 0.3 g kg^{-1} (0.05 g kg^{-1}). The thick dashed lines indicate 0, -15, and -25 m s^{-1} relative to the ground. D1, D2, D3 and ''D4'' indicate westward-propagating disturbances.

horizontally with remaining region R. Its upward motion then promotes the growth of shallow convection into long-lived convective band B3 at $x = -305$ km (Figs. 7e and 7f).

Figure 9 shows the vertical cross section of wind vectors superimposed on temperature perturbation at $t = 390$ min just after the dissipation of cell C. The wind vectors and temperature perturbation were extracted by using a bandpass filter with cutoff horizontal wavelengths of 10 and 30 km. In this figure, the antinode and node of vertical velocity are clearly seen at $z = 6$ and 10 km. Maximum (minimum) in temperature perturbations is centered one-quarter wavelength ahead of (i.e., to the left of) the updraft (the downdraft) at $z = 6$ km. In addition, the updraft is located one-quarter wavelength behind a maxima in horizontal wind perturbations below and a minimum in horizontal wind perturbations above. A vertically standing structure with the above quadrature relationship indicates that disturbance D3 is a ducted gravity wave, and thus could reach shallow convection at $x = -305$ km without propagating into the middle atmosphere. The vertical wave length is calculated as about 16 km.

The wave parameters for disturbance D3 can be roughly estimated from the linear dispersion relation for internal gravity waves under the Boussinesq approximation as

$$m^2 = \frac{N^2}{(U - c_x)^2} - \frac{d^2U/dz^2}{U - c_x} - k^2 \qquad (2)$$

where m ($=2\pi/L_z$) is the vertical wave number, k ($=2\pi/L_x$) the horizontal wave number, and U the background wind speed. The vertical profiles of the horizontal wind relative to the ground U (m s^{-1}) and the square of the Brunt–Väisälä frequency N^2 (s^{-2}) averaged from $x = -300$ km to $x = -260$ km at $t = 360$ min before the passages of disturbance D3 are shown in Fig. 10. The Brunt–Väisälä frequency is calculated for saturated fair, following Durran and Klemp [1982, see their Eq. (36)]. From the soundings shown in Fig. 10, N^2 (9.9×10^{-5} s^{-2}), U (-2.9 m s^{-1}) and d^2U/dz^2 (-9.2×10^{-8} m^{-1} s^{-1}) are obtained by averaging from $z = 2.0$ km to $z = 14.5$ km. For a horizontal phase speed $c_x = -24$ to -27 m s^{-1} and a horizontal wavelength $L_x = 20$ to 21 km, vertical wavelength L_z is calculated from (2) as 18 to 22 km, in fair accord with the result from Fig. 9. This result confirms that westward-propagating disturbance

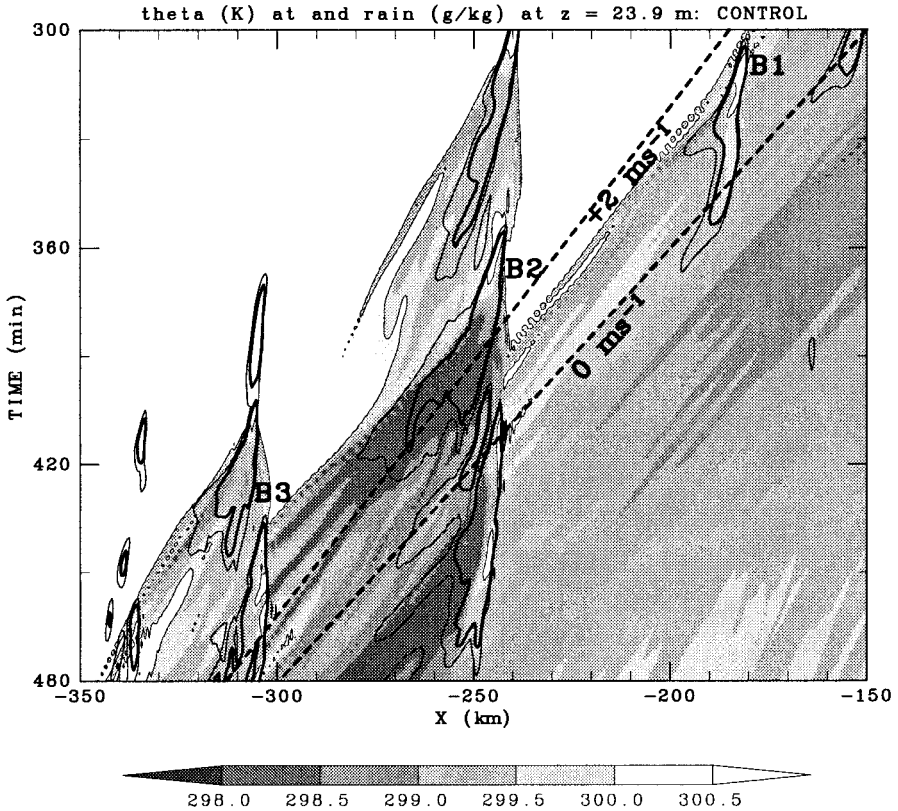

FIG. 6. As in Fig. 5 but for potential temperature (K) and rain mixing ratio (g kg^{-1}) at $z = 23.9$ m in the CONTROL case. The degree of shading denotes the range of potential temperature, as indicated by the value bar at the bottom of the figure. The heavy (light) solid lines indicate the region in which the rain mixing ratio exceeds 0.3 g kg^{-1} (0.05 g kg^{-1}). The thick dashed lines indicate 0 and +2 m s^{-1} relative to the ground.

D3 is a gravity wave. The increasing rate of easterly wind shear ($-d^2U/dz^2$) used for calculating the vertical wavelength is possibly underestimated by averaging from $z = 2.0$ km to $z = 14.5$ km, so the calculated vertical wavelength may be overestimated. In the same way for the disturbance D3, vertical wavelength L_z of disturbance D1 is calculated as 11 to 12 km, in fair accord with the estimated value of 12 km from the vertical cross section (not shown).

4. Discussions

a. Wave excitation below the convective cell

Fovell et al. (1992), using a two-dimensional numerical model, demonstrated that the high-frequency stratospheric gravity waves propagating upward and opposite to the direction of the motion of the storm are preferentially excited by a mesoscale convective storm. They attributed the preferential excitation of rearward-propagating waves to the rearward storm-relative motion of convective cells. Although the preferential excitation of the westward-propagating waves in CONTROL is similar to that in Fovell et al. (1992), the waves in CONTROL propagate below the convective cells in contrast to the waves in Fovell et al. (1992) propagating upward.

To investigate preferential excitation mechanisms of westward-propagating waves below the convective cell, we conducted a series of simulations in which gravity waves are excited by thermal forcing (''DRY''). The model is the same as that used in the CONTROL case except for a constant vertical resolution of 500 m and exclusions of cloud microphysics and the model-domain translation. The static stability profile has a constant Brunt–Väisälä frequency N ($=0.01$ s^{-1}). The horizontal wind profile examined in the DRY0 and DRY1 cases is shown in Fig. 11. The wind speed is set to 0 m s^{-1} below $z = 5$ km and easterly shear of 4 m s^{-1} per 1 km above $z = 5$ km, which is a simplified wind profile in the CONTROL case. In the DRY2 case, the wind speed is set to 0 m s^{-1} in the whole domain. The thermal forcing function is given as

$$Q(x, z, t) = Q_0 \frac{1}{[1 + (x - x_0)^2/a^2 + (z - z_0)^2/a^2]^{3/2}} \times \frac{1 - \cos(2\pi t/T)}{2}, \quad (3)$$

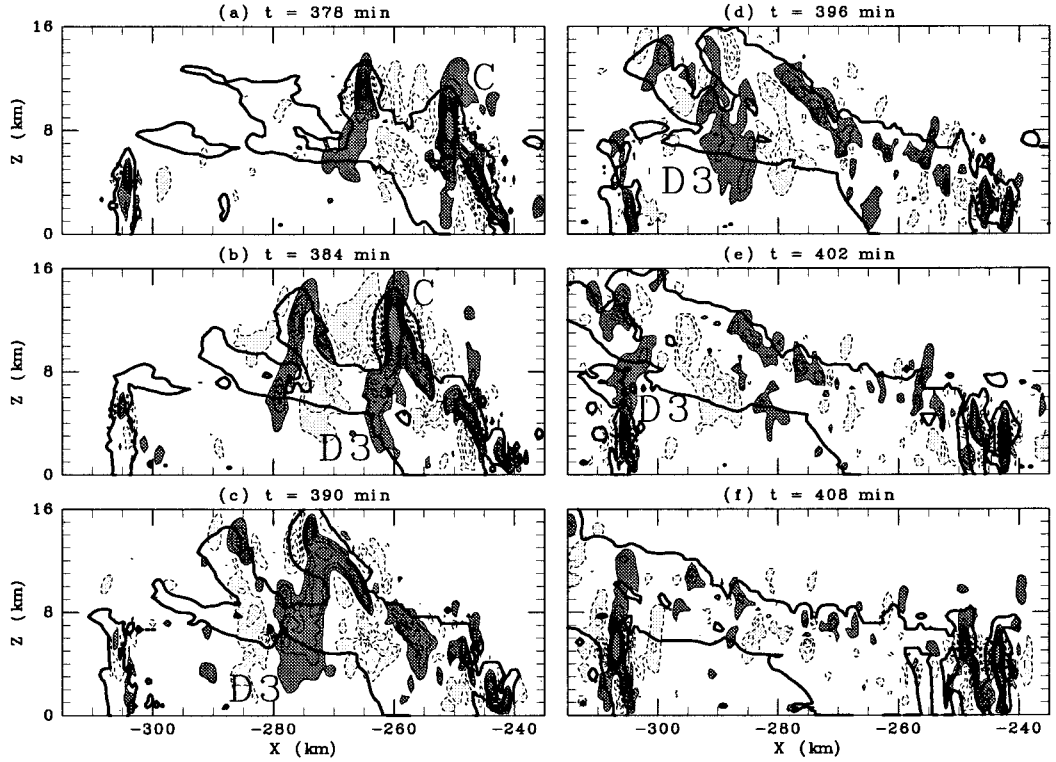

FIG. 7. Time sequence of vertical cross sections of vertical velocity (contour interval 1.0 m s^{-1}) superposed on cloud outline (bold line), defined as the region in which the mixing ratio of condensates exceeds 0.1 g kg^{-1}, for the CONTROL case. Positive (negative) values are solid (dashed). Updraft greater than 1.0 m s^{-1} is heavily shaded, and downdraft less than -1.0 m s^{-1} is lightly shaded. C indicates an old convective cell separating from the leading edge of band B2 at $x = -240$ km.

where the magnitude of the thermal forcing $Q_0 = 1$ J kg^{-1}, the half-width $a = 1$ km, $T = 10$ min,

$$x_0 = \begin{cases} H\dfrac{dU}{dz}\dfrac{2T}{\pi}\left[1 - \cos\left(\dfrac{\pi t}{2T}\right)\right] + x_s & \text{DRY0} \\ U_c t + x_s & \text{DRY1} \\ x_s & \text{DRY2} \end{cases} \quad (4)$$

and

$$z_0 = \begin{cases} H \sin\left(\dfrac{\pi t}{2T}\right) + z_s & \text{DRY0} \\ z_c & \text{DRY1} \\ H \sin\left(\dfrac{\pi t}{2T}\right) + z_s & \text{DRY2.} \end{cases} \quad (5)$$

Here $dU/dz = -4 \times 10^{-3}$ s^{-1}, $x_s = 0$ km, $z_s = 5$ km, $H = 10$ km, $z_c = 10$ km, and $U_c = -20$ m s^{-1}.

In DRY0, the source function has the form of an ascending and westward-accelerated thermal restricted to a small region in space centered at (x_0, z_0). The horizontal velocity of the ascending thermal is the same as that of the wind at $z_0(t)$. This form of source function approximates the characteristics of the convective cell separating from the leading edge of a multicell storm; it ascends with westward acceleration and then dissipates. The DRY1 and DRY2 cases are conducted to examine the role of westward motion and ascending of the forcing in the preferential generation of the westward-propagating wave below the cell. In DRY1, the thermal forcing is fixed at a constant height, but it moves westward. In DRY2, the thermal forcing is fixed in the x direction, but it ascends until $z = 15$ km the same as in DRY0.

The vertical velocity at $t = 10$ min in the DRY0 case is shown in Fig. 12b. A strong updraft is seen at $x = -13$ km and $z = 13$ km. Below this strong updraft, upward motion is produced upstream relative to the thermal forcing (to the west). This pattern of updraft is similar to that in the CONTROL case (Fig. 12a).

Figures 12c and 12d show the vertical velocity at $t = 10$ min in DRY1 and DRY2, respectively. In DRY1, the disturbances with upward motion are produced upstream both below and above the forcing. These disturbances in DRY1 propagate westward relative to the ground. In DRY2, upward motion below the forcing is preferentially generated. The response in DRY2 is, however, symmetric about the forcing. These results suggest that two factors contribute to preferential generation of westward-propagating waves below the cell (forcing) in

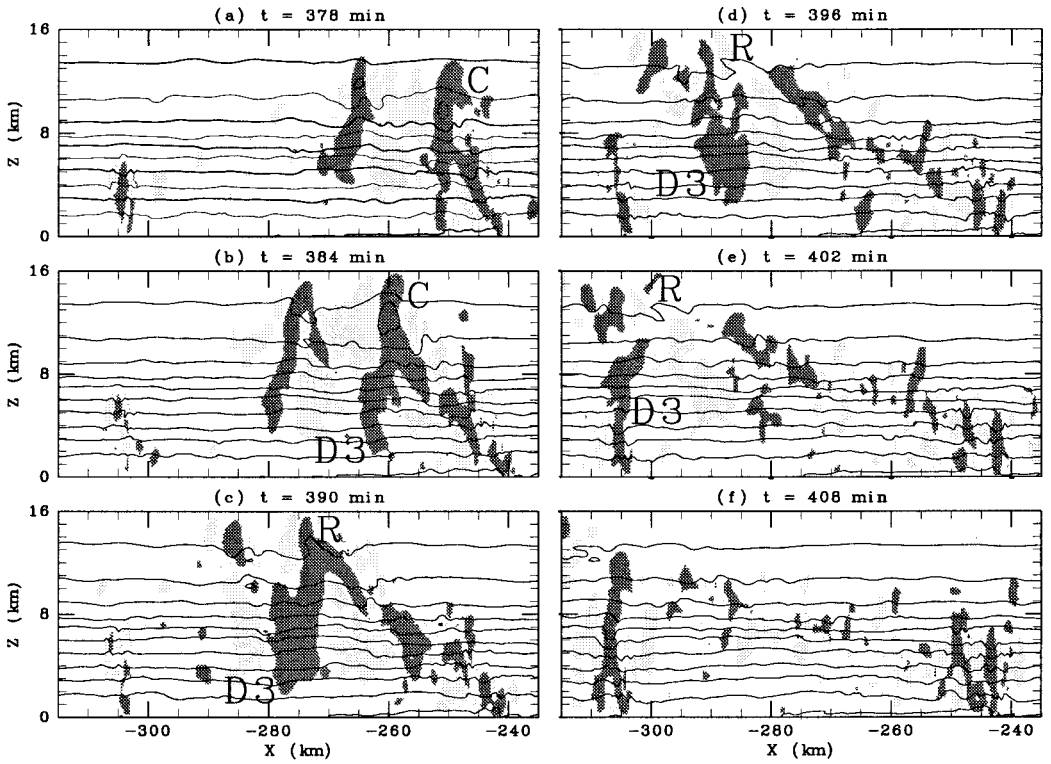

FIG. 8. As in Fig. 7 but for vertical velocities and potential temperature (contour interval 5 K). Updraft greater than 1.0 m s^{-1} is heavily shaded, and downdraft less than -1.0 m s^{-1} is lightly shaded. R indicates the remaining unstable region of cell C.

CONTROL and DRY0: westward motion of the cell excites westward-propagating waves, and ascension of the cell excites waves below the cell.

Generally, the phase of the wave locks onto the motion of the forcing in a steady state. Thus waves excited by a westward-moving source naturally propagate westward. Lin and Li (1988), investigating the steady response of the atmosphere to an elevated stationary heat source, showed that the wave energy propagates downward and upstream relative to the air in an unbounded steady shear flow, but is advected downstream by the basic flow. The wave activity is thus found downstream relative to the source, which is similar to the mountain wave. In contrast to Lin and Li (1988), the wave activity

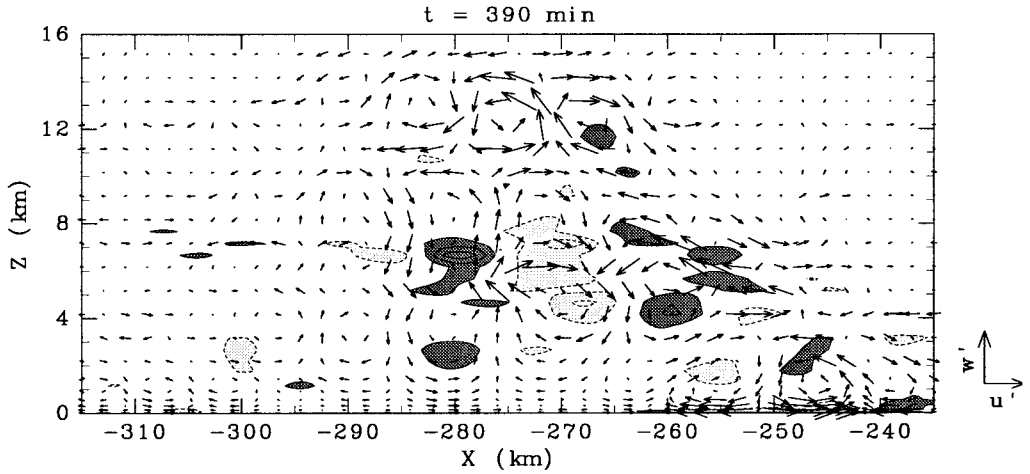

FIG. 9. Vertical cross section of wind vectors and temperature perturbation (contour interval 0.5 K) at $t = 390$ min for the CONTROL case. Rightward and upward unit vectors show horizontal wind (u') and vertical velocity (w') perturbations of 1.0 m s^{-1}, respectively. Temperature perturbations greater than 0.5 K (less than -0.5 K) are heavily (lightly) shaded. The wind vectors and temperature perturbation are extracted by using a bandpass filter with cutoff horizontal wavelengths of 10 and 30 km.

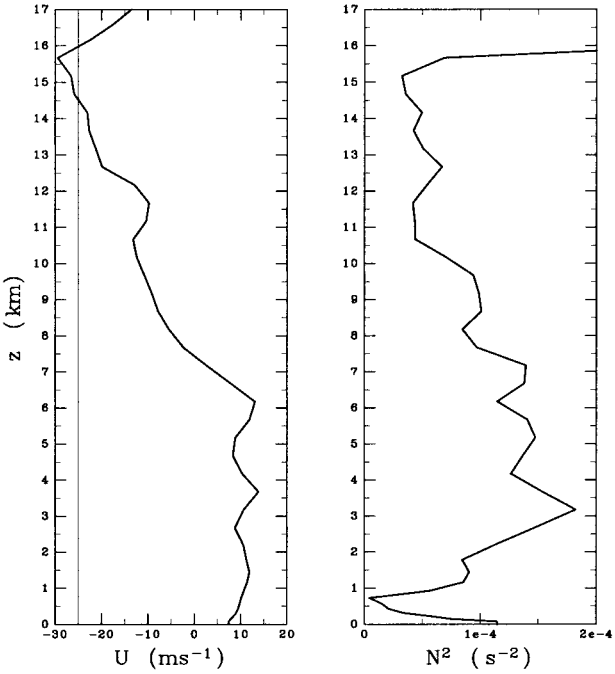

FIG. 10. (left) Vertical profiles of horizontal wind relative to the ground and (right) square of the Brunt–Väisälä frequency averaged from $x = -300$ km to $x = -260$ km at $t = 360$ min for the CONTROL case. The thin vertical line in the left panel indicates U = −25 m s^{-1}.

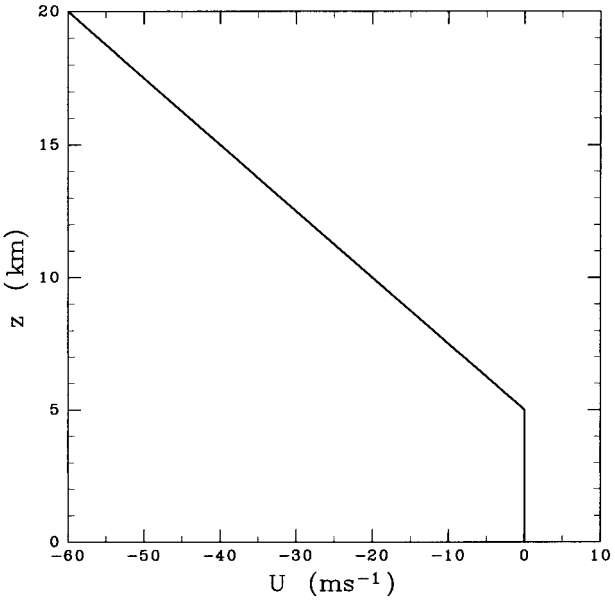

FIG. 11. Initial wind profile for DRY0 and DRY1.

is found upstream relative to the source in CONTROL and DRY0. Studies on the transient response of the atmosphere to a spatially and temporally localized heat source showed that, when the intensity of the heat source decays, upward motion develops in the adjacent region and propagates outward as a gravity wave (e.g., Nicholls et al. 1991; Shige and Satomura 2000); therefore, the phase of the disturbance does not lock onto the source. Since the intensity of the heat source in CONTROL and

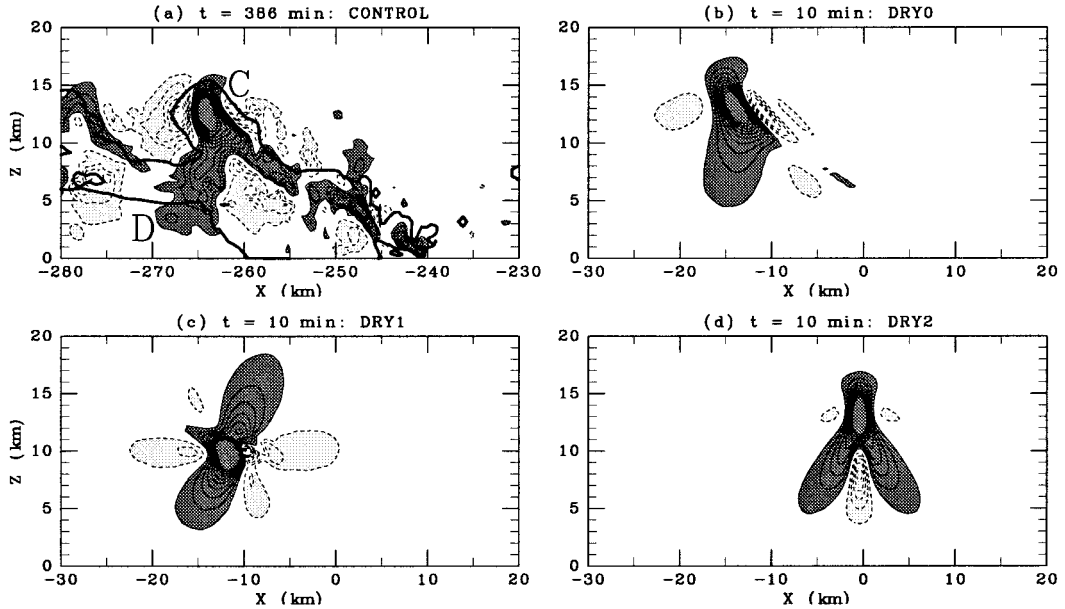

FIG. 12. (a) As in Fig. 7 but for $t = 386$ min in CONTROL. Vertical cross section of vertical velocity (contour interval 0.01 m s^{-1}) in (b) DRY0, (c) DRY1, and (d) DRY2. Positive (negative) values are solid (dashed). Updraft greater than 0.01 m s^{-1} is heavily shaded, and downdraft less than −0.01 m s^{-1} is lightly shaded.

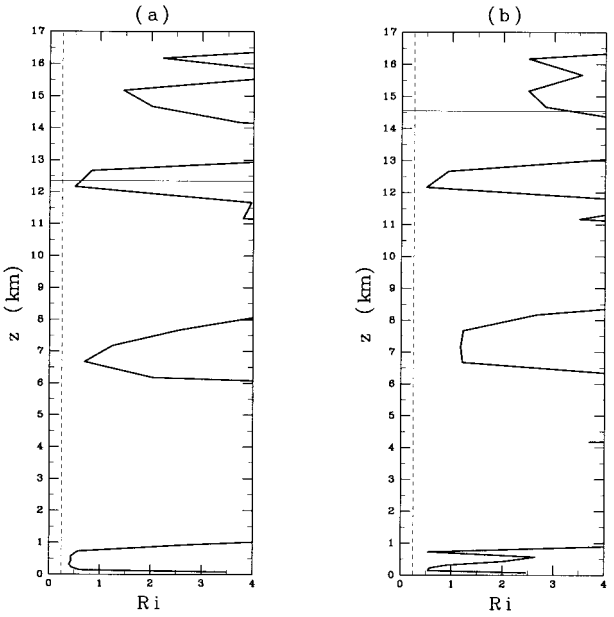

FIG. 13. Vertical profiles of the Richardson number Ri averaged (a) from $x = -240$ km to $x = -200$ km at $t = 300$ min before the passage of disturbance D1 and (b) from $x = -300$ km to $x = -260$ km at $t = 360$ min before the passage of disturbance D3 for the CONTROL case. The thin lines indicate the levels of the mean wind speed of (a) -15 m s^{-1} and (b) -25 m s^{-1}. The dotted lines indicate the Richardson number value of 0.25.

DRY0 decayed, the wave energy could propagate upstream relative to the source as a transient response to the decaying source.

In contrast, for an ascending source, the phases of the excited waves propagate upward. The vertical group velocity has a sign opposite to the vertical phase speed. Thus, for an ascending source, waves with upward phase propagation should be observed below the source because their energy propagates downward. In CONTROL and DRY0, the wave activity was, therefore, found below the source.

The dominant horizontal phase speeds of excited waves near their source region deeply depend on the moving speed of their source. Waves of fast (slow) horizontal phase speed are excited by a fast (slow) moving source. In deeper bands (later B2 and later B3; Figs. 4b and c), convective cells ascend higher and are accelerated by stronger easterlies; thus they generate fast-propagating waves (D3 and D4; Fig. 5). In shallower bands (B1 and earlier B2; Fig. 4a), convective cells ascend lower and are accelerated by weaker easterlies; thus they generate slow-propagating waves (D1 and D2; Fig. 5).

b. Wave duct

Lindzen and Tung (1976) proposed four conditions necessary for a duct in which gravity waves are trapped: 1) a statically stable duct layer, in which gravity waves could propagate, is adjacent to the ground; 2) the duct is deeper than one quarter of the vertical wavelength of the gravity waves; 3) the duct is topped by an unstable layer of Richardson number Ri$[=N^2/(dU/dz)^2] < 0.25$; and 4) the unstable layer contains a critical level where the mean wind speed is equal to, or nearly equal to, the ground-relative phase speed of the gravity wave.

As shown in Fig. 10, the mean profile of N^2 below $z = 10$ km is favorable for wave propagation. The vertical profile of Richardson number Ri averaged from $x = -240$ km to $x = -200$ km at $t = 300$ min before the passage of disturbance D1 is shown in Fig. 13a. The critical level at $z = 12.3$ km where the mean wind speed (-15 m s^{-1}) is nearly equal to the phase speed of disturbance D1 (-15 to -16 m s^{-1}) is illustrated by the horizontal thin line in Fig. 13. Although the layer containing the critical level has Ri > 0.25, the Richardson number is small (about 0.5). Disturbance D1 is consid-

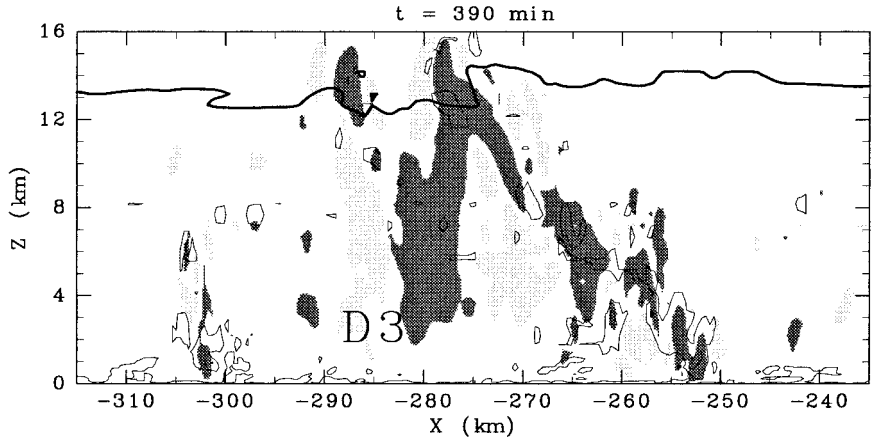

FIG. 14. As in Fig. 9 but for regions having Ri < 0.25 (contour) superposed on vertical velocity field at $t = 390$ min for the CONTROL case. A bold line indicates the critical levels where the horizontal wind (-25 m s^{-1}) is nearly equal to the phase speed of disturbance D3 (-24 to -27 m s^{-1}). Updrafts greater than 1.0 m s^{-1} are heavily shaded, and downdrafts less than -1.0 m s^{-1} are lightly shaded.

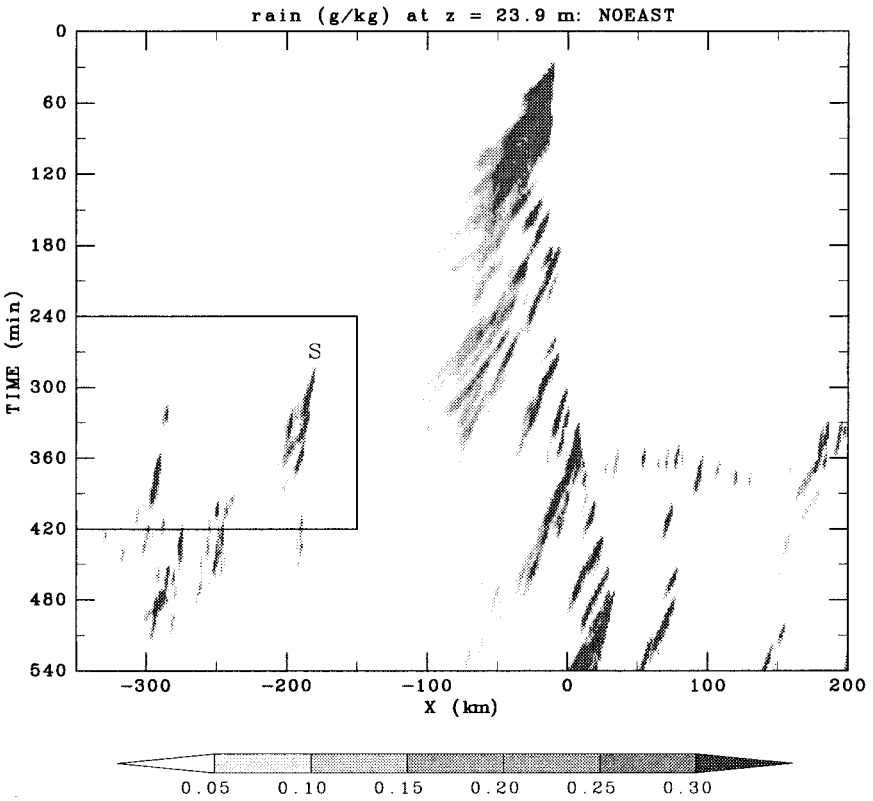

FIG. 15. As in Fig. 3 but for the NOEAST case. The rectangle indicates the region that is expanded in Fig. 16. S indicates a precipitating band.

ered to be trapped in the troposphere because the ducting conditions proposed by Lindzen and Tung (1976) are roughly satisfied.

The vertical profile of the Richardson number averaged from $x = -300$ km to $x = -260$ km at $t = 360$ min before the passage of disturbance D3 is shown in Fig. 13b. The critical level at $z = 14.5$ km where the mean wind speed (-25 m s^{-1}) is nearly equal to the phase speed of disturbance D3 (-24 to -27 m s^{-1}) is illustrated by the horizontal thin line in Fig. 13b. It is clear from this figure that the layer containing the critical level has a large Richardson number (about 3.0). According to Booker and Bretherton's theory (1967), waves should be absorbed by the critical level for a large Richardson number flow.

Figure 14 shows the regions having Ri < 0.25 superposed on the vertical velocity field at $t = 390$ min just after the dissipation of cell C. A local region having Ri < 0.25 at $x = -280$ to -275 km just above disturbance D3 is noticed around the critical levels where the horizontal wind (-25 m s^{-1}) is nearly equal to the phase speed of the disturbance D3 in Fig. 14. This region with Ri < 0.25 is remaining region R (Fig. 8c) of convective cell C that excited disturbance D3 and dissipated near $z = 14.5$ km. Remaining region R is passively advected by the mean flow near the equilibrium level ($z = 14.5$ km). Thus, disturbance D3, with a horizontal phase speed that happens to match the mean flow near the equilibrium level, is trapped in the troposphere owing to remaining region R because the ducting conditions proposed by Lindzen and Tung (1976) are locally satisfied. Lindzen (1988) noted that, for the reflection of a wave, the wave must tunnel through the layer of Ri < 0.25 to reach the critical level, thus the layer of Ri < 0.25 must not be too deep. Therefore, the shallowness of remaining region R is rather favorable for the trapping and reflection of the wave.

For the slow-propagating waves generated by the shallow bands (B1 and earlier B2) whose heights are less than 12 km, waves (D1 and D2) having their critical levels within the small Richardson number layer at $z = 12$ km are ducted. The ducting situation of the slow-propagating mode is similar to that in Shige (1999). On the other hand, for fast-propagating waves (D3 and D4) generated by the deep bands (later B2 and B3) whose heights exceed than 12 km, waves (D3 and D4) having their critical levels within the remaining region of convective cells are ducted.

c. Effect of strong easterlies aloft

In order to examine the effect of the strong easterlies aloft on the westward generation of new convective bands, we performed an experiment with a wind profile

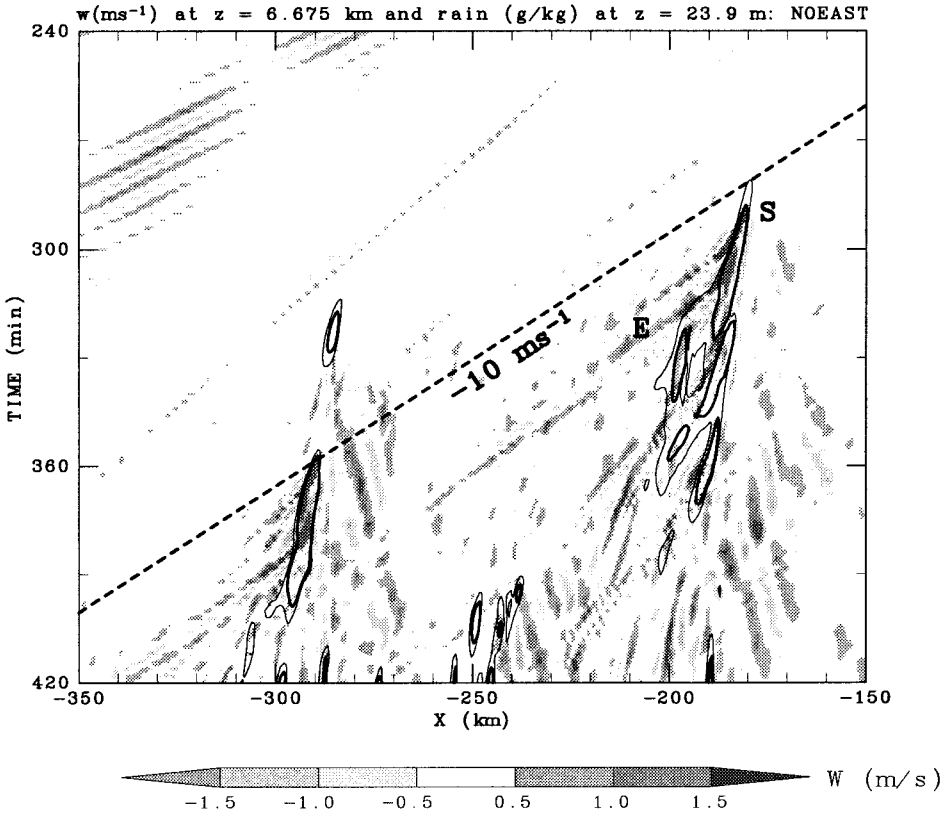

FIG. 16. As in Fig. 5 but for the NOEAST case, illustrating an expanded view of the rectangle in Fig. 15. The thick dashed line indicates -10 m s^{-1} relative to the ground. E indicates a westward-propagating disturbance.

in which easterlies aloft are reduced (NOEAST). The initial wind profile used in the NOEAST case is shown Fig. 2. The wind speed in the NOEAST case is 0 m s^{-1} relative to the ground above $z = 11$ km. Figure 15 shows a time-zonal section of the mixing ratio of rain at $z = 23.9$ m in the NOEAST case. Discrete generation of new convective bands to the west of an old convective band is much weaker than the CONTROL case.

An expanded view of the rectangle in Fig. 15 is illustrated in Fig. 16, which shows a time-zonal cross section of vertical velocity at $z = 6.675$ km and mixing ratio of rain at $z = 23.9$ m. Band S remained nearly stationary at $x = -180$ km in the moving frame. The time-zonal cross section of potential temperature (not shown) indicates that band S was initiated by the cold pool spreading rearward from the primary band initiated by the thermal bubble, the same as band B1 in the CONTROL case. Band S was also a short-lived band, confirming that the cold pool spreading rearward from the primary band cannot develop long-lived bands. Westward-propagating disturbance E has horizontal phase speed $c_x = -9$ to -10 m s^{-1} relative to the ground, and horizontal wavelength $L_x = 11$ to 12 km. The vertical wave length is calculated as 8 to 9 km. Disturbance E does not promote the development of convection to the west of band S.

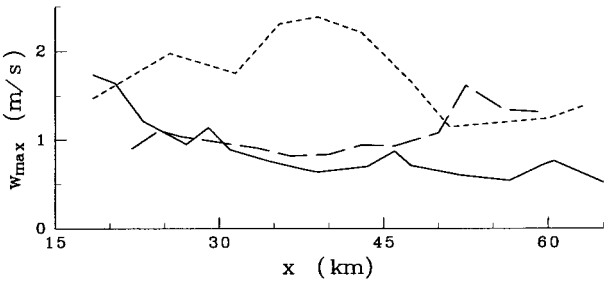

FIG. 17. Peak vertical velocities associated with disturbances D1 (dotted), D3 (dashed), and E (solid). The horizontal axis indicates the horizontal distance from the leading edge of the bands that excited waves.

Figure 17 shows the peak vertical velocities associated with disturbances D1, D3, and E. Vertical velocities for disturbances D1, D2, and E were extracted by using bandpass filters with cutoff horizontal wavelengths of 10 and 30 km (D1), 6 and 18 km (D2), and 5 and 15 km (E). Disturbances D1 and D3 still have peak vertical velocities exceeding 1.0 m s^{-1} even after they propagate horizontally about 60 km from the bands that excited them. In contrast, the peak vertical velocity of disturbance E is less than 1.0 m s^{-1} when it propagates about 60 km from the band that excited it. Thus, even if a shallow convection exists to the west of band S, dis-

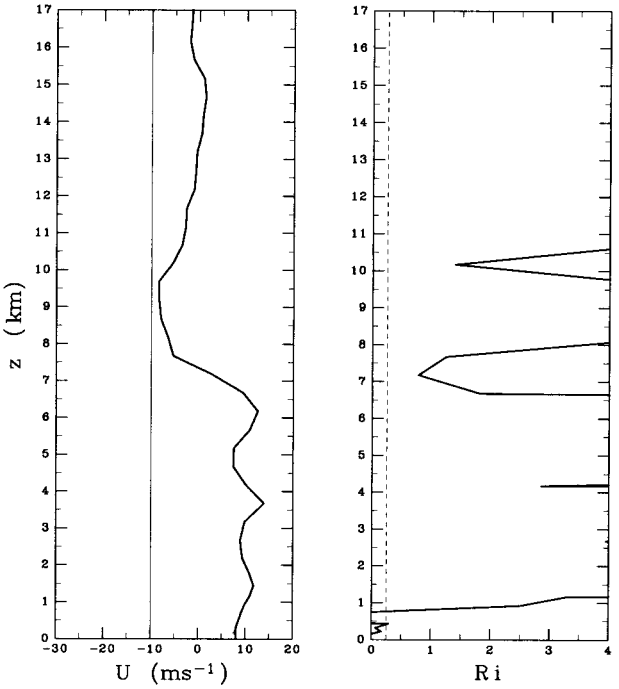

FIG. 18. (left) Vertical profiles of horizontal wind relative to the ground and (right) Richardson number Ri averaged from $x = -250$ km to $x = -210$ km at $t = 270$ min for the NOEAST case. The thin vertical line in the left panel indicates U $= -10$ m s^{-1}. The dotted lines indicates Ri $= 0.25$.

turbance E cannot promote its growth to a long-lived band.

The vertical profile of horizontal wind speed relative to the ground U (m s^{-1}) and Richardson number Ri averaged from $x = -250$ km to $x = -210$ km at $t = 270$ min before the passages of disturbance E are shown in Fig. 18. There are no critical levels of disturbance E, although there is a relatively small Richardson number layer at $z = 10$ km. Thus disturbance E is not trapped and loses its energy. These results confirm that strong easterlies are very important for discrete generation of a new convective band to the west of an old convective band in the CONTROL case.

As mentioned in the Introduction, Mori (1995) and Lewis et al. (1998) also reported generation of a new convective band to the west of an old convective band in TOGA COARE. The wind profile characterized by west winds at low levels and strong easterlies aloft (~20 m s^{-1}) is common to these cases (see Fig. 2 of Mori 1995, and Figs. 5 and 6 of Lewis et al. 1998). The strong easterlies are likely to match the phase speeds of the westward-propagating gravity waves generated by eastward-moving convective bands. Thus, these cases are also possibly explained by the convectively generated gravity wave mechanism proposed in this paper.

The typical zonal wind in the convectively active phase of the ISO during TOGA COARE was characterized by strong easterlies aloft with low-level westerlies (Lin and Johnson 1996). Murakami and Wang (1993), using 10 years of data for outgoing long radiation (OLR) and 8 years of data for 200-mb winds, showed that easterlies in the equatorial upper troposphere are strongest above the convective center over the maritime continent (100°–150°E). Their results indicate that the climatic wind profile in this area favors the trapping of westward-propagating gravity waves in the troposphere. Thus, we consider that westward generation of new convective bands by ducted gravity waves occurs in convectively active regions over the equatorial western Pacific.

5. Summary and concluding remarks

Mechanisms responsible for westward generation of eastward-moving tropical convective bands over the equatorial western Pacific were investigated using a numerical cloud model. A simulation was initialized with the sounding of R/V *Vickers* on 11 February 1993 during TOGA COARE, with west winds at low levels and easterlies aloft. It was a convectively active day on which discrete generation of a new convective band to the west of an eastward-moving convective band was observed (Halverson et al. 1999).

In this paper, the westward generation of new convective bands was explained by a gravity wave mechanism. Two westward-propagating modes excited below cells moving rearward relative to eastward-moving convective bands appeared to play an important role. A slow-propagating mode (~15 m s^{-1}) was ducted in the troposphere owing to an unstable layer of small Richardson number containing its critical level (Fig. 19a). The slow-propagating mode was excited by the cell in a shallow convective band whose height was less than the unstable layer. A fast-propagating mode (~25 m s^{-1}) was excited by the cell in a deep convective band whose height exceeded than the unstable layer (Fig. 19b). The fast-propagating mode was ducted in the troposphere owing to the remaining region of the cell containing its critical level (Fig. 19c). These two modes thus propagated horizontally with no significant energy leak into the stratosphere and promoted the growth of shallow convections into long-lived convective bands.

In order to investigate preferential excitation mechanisms of westward-propagating waves below the cell (Fig. 19b), we conducted a series of simulations in which gravity waves were excited by a thermal forcing representing the cell (''DRY''). These simulations showed that preferential excitation of westward-propagating waves was due to westward motion of the cell, while that of waves below the cell was due to ascension of the cell.

A comparative simulation (NOEAST) showed that a new convective band was not generated to the west of an old convective band when the critical level was removed. This result confirms strong easterlies are very

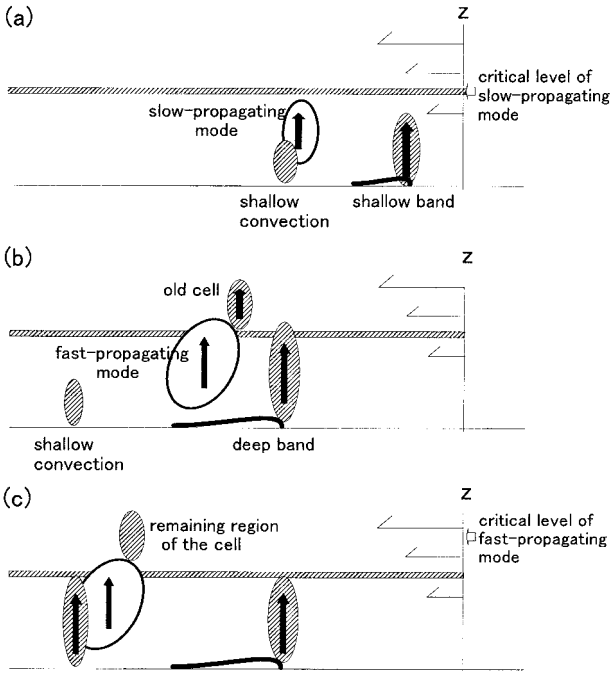

FIG. 19. A schematic model for generation of a new convective band to the west of an old convective band in a moving frame. Solid arrows indicate upward motion. Bold lines indicate cold pool outlines. The regions of small Richardson number ($<=0.25$) are shaded. (a) A slow-propagating mode, which has its critical level within the small Ri layer, propagates horizontally and promotes the growth of shallow convection to a long-lived convective band. (b) A fast-propagating mode is excited below an old convective cell in a deep convective band whose height is higher than the small Ri layer. (c) The fast-propagating mode, which has its critical level within the remaining region of the cell, propagates horizontally and promotes the growth of shallow convection into a long-lived convective band.

important for discrete generation of a new convective band to the west of an old convective band.

Acknowledgments. Discussions with Mr. Noriyuki Nishi and Dr. Toru Terao, and comments by Dr. Takeshi Horinouchi, are greatly appreciated. We thank Drs. George N. Kiladis and Mitchell W. Moncrieff and an anonymous reviewer for their helpful reviews of this manuscript, and Drs. Timothy J. Dunkerton and Kazuyoshi Oouchi for additional comments. The simulations were made using the Regional Atmospheric Modeling System (RAMS) developed at Colorado State University. GFD-DENNOU was utilized for graphics. This work was supported by a research fellowship from the Japan Society for the Promotion of Science for Young Scientists (SS).

REFERENCES

Alexander, G. D., and G. S. Young, 1992: The relationship between EMEX mesoscale precipitation feature properties and their environmental characteristics. *Mon. Wea. Rev.,* **120,** 554–564.

Barnes, G. M., and K. Sieckman, 1984: The environment of fast- and slow-moving tropical mesoscale convective cloud lines. *Mon. Wea. Rev.,* **112,** 1782–1794.

Booker, J. R., and F. P. Bretherton, 1967: The critical layer for internal gravity waves in a shear layer. *J. Fluid Mech.,* **27,** 513–559.

DeMott, C. A., and S. A. Rutledge, 1998: The vertical structure of TOGA COARE convection. Part I: Radar echo distribution. *J. Atmos. Sci.,* **55,** 2730–2747.

Durran, D. R., and J. B. Klemp, 1982: On the effects of moisture on the Brunt–Väisälä frequency. *J. Atmos. Sci.,* **39,** 2152–2158.

Emanuel, K. E., 1987: An air interaction model of intraseasonal oscillations in the tropics. *J. Atmos. Sci.,* **44,** 2324–2340.

Fovell, R. G., and Y. Ogura, 1988: Numerical simulation of a midlatitude squall line in two dimensions. *J. Atmos. Sci.,* **45,** 3846–3879.

——, D. R. Durran, and J. R. Holton, 1992: Numerical simulations of convectively generated stratospheric gravity waves. *J. Atmos. Sci.,* **49,** 1427–1442.

Halverson, J. B., B. S. Ferrier, T. M. Rickenbach, J. Simpson, and W.-K. Tao, 1999: An ensemble of convective systems on 11 February 1993 during TOGA COARE: Morphology, rainfall characteristics, and anvil cloud interactions. *Mon. Wea. Rev.,* **127,** 1208–1228.

Johnson, R. H., T. M. Rickenbach, S. A. Rutledge, P. E. Ciesielski, and W. H. Schubert, 1999: Trimodal characteristics of tropical convection. *J. Climate,* **12,** 2397–2418.

Klemp, J., and R. Wilhelmson, 1978: The simulation of three-dimensional convective storm dynamics. *J. Atmos. Sci.,* **35,** 1070–1096.

Lafore, J. P., and M. W. Moncrieff, 1989: A numerical investigation of the organization and interaction of the convective and stratiform regions of tropical squall lines. *J. Atmos. Sci.,* **46,** 521–544.

LeMone, M. A., E. J. Zipser, and S. B. Trier, 1998: The role of environmental shear and thermodynamics conditions in determining the structure and evolution of mesoscale convective system during TOGA COARE. *J. Atmos. Sci.,* **55,** 3493–3518.

Lewis, S. A., M. A. LeMone, and D. P. Jorgensen, 1998: Evolution and dynamics of a late-stage squall line that occurred on 20 February 1993 during TOGA COARE. *Mon. Wea. Rev.,* **126,** 3189–3212.

Lin, X., and R. H. Johnson, 1996: Kinematic and thermodynamic characteristics of the flow over the western Pacific warm pool during TOGA COARE. *J. Atmos. Sci.,* **53,** 695–715.

Lin, Y.-L., and S. Li, 1988: Three-dimensional response of a shear flow to elevated heating. *J. Atmos. Sci.,* **45,** 2987–3002.

Lindzen, R. S., 1988: Instability of plane parallel shear flow (toward a mechanistic picture of how it works). *PAGEOPH,* **126,** 103–121.

——, and K. K. Tung, 1976: Banded convective activity and ducted gravity waves. *Mon. Wea. Rev.,* **104,** 1602–1617.

Louis, J. F., 1979: A parametric model of vertical eddy fluxes in the atmosphere. *Bound.-Layer Meteor.,* **17,** 187–202.

Madden, R. A., and P. Julian, 1971: Detection of a 40–50-day oscillation in the zonal wind in the tropical Pacific. *J. Atmos. Sci.,* **28,** 702–708.

Mapes, B. E., 1993: Gregarious tropical convection. *J. Atmos. Sci.,* **50,** 2026–2037.

Matsuno, T., 1966: Quasi-geostrophic motions in the equatorial area. *J. Meteor. Soc. Japan,* **44,** 25–43.

McAnelly, R. L., J. E. Nachamkin, W. R. Cotton, and M. E. Nicholls, 1997: Upscale evolution of MCSs: Doppler radar analysis and analytical investigation. *Mon. Wea. Rev.,* **125,** 1083–1110.

Moncrieff, M. W., and C. Liu, 1999: Convection initiation by density currents: Role of convergence, shear, and dynamical organization. *Mon. Wea. Rev.,* **127,** 2455–2464.

Mori, K., 1995: Equatorial convection observed by the research vessel Keifu Maru during the TOGA COARE IOP, November 1992. *J. Meteor. Soc. Japan,* **73,** 491–508.

Murakami, T., and B. Wang, 1993: Annual cycle of equatorial east–

west circulation over the Indian and Pacific oceans. *J. Climate,* **6,** 932–952.

Nakazawa, T., 1988: Tropical super clusters within intraseasonal variations over the western Pacific. *J. Meteor. Soc. Japan,* **66,** 823–839.

Neelin, J. D., I. M. Held, and K. H. Cook, 1987: Evaporation-wind feedback and low-frequency variability in the tropical atmosphere. *J. Atmos. Sci.,* **44,** 2341–2348.

Nicholls, M. E., R. A. Pielke, and W. R. Cotton, 1991: Thermally forced gravity waves in an atmosphere at rest. *J. Atmos. Sci.,* **48,** 2561–2572.

Oouchi, K., 1999: Hierarchical organization of super cloud cluster cased by WISHE, convectively induced gravity waves and cold pool. *J. Meteor. Soc. Japan,* **77,** 907–927.

Pandya, R. E., and D. R. Durran, 1996: The influence of convectively generated thermal forcing on the mesoscale circulation around squall lines. *J. Atmos. Sci.,* **53,** 2924–2951.

——, ——, and C. S. Bretherton, 1993: Comments on ''Thermally forced gravity waves in an atmosphere at rest.'' *J. Atmos. Sci.,* **50,** 4098–4101.

——, ——, and M. L. Weiseman, 2000: The influence of convective thermal forcing on the three-dimensional circulation around squall lines. *J. Atmos. Sci.,* **57,** 29–45.

Parsons, D., and Coauthors, 1994: The Integrated Sounding System: Description and preliminary observations from TOGA COARE. *Bull. Amer. Meteor. Soc.,* **75,** 553–567.

Rickenbach, T. M., and S. A. Rutledge, 1998: Convection in TOGA COARE: Horizontal scale, morphology, and rainfall production. *J. Atmos. Sci.,* **55,** 2715–2279.

Rotunno, R., J. B. Klemp, and M. L. Weisman, 1988: A theory for strong, long-lived squall lines. *J. Atmos. Sci.,* **45,** 463–485.

Shige, S., 1999: Disturbances of 1–2-hour periods observed in the tropical lower troposphere during the TOGA-COARE IOP. *J. Meteor. Soc. Japan,* **77,** 1123–1136.

——, and T. Satomura, 2000: The gravity wave response in the troposphere around deep convection. *J. Meteor. Soc. Japan,* **78,** 789–801.

Takayabu, Y. N., 1994: Large-scale cloud disturbances associated with equatorial waves. Part II: Westward-propagating inertio-gravity waves. *J. Meteor. Soc. Japan,* **72,** 451–465.

Tao, W.-K., and J. Simpson, 1989: Modeling study of a tropical squall-type convective line. *J. Atmos. Sci.,* **46,** 177–202.

Wada, K., T. Nitta, and K. Sato, 1999: Equatorial inertia-gravity waves in the lower stratosphere revealed by TOGA-COARE IOP data. *J. Meteor. Soc. Japan,* **77,** 721–736.

Webster, P. J., and R. Lukas, 1992: TOGA COARE: The coupled ocean–atmosphere response experiment. *Bull. Amer. Meteor. Soc.,* **73,** 1377–1416.

Yoshizaki, M., 1991: On the selection of eastward-propagating modes appearing in the wave-CISK model as tropical intraseasonal (30–60-day) oscillations—Linear responses to localized heating in the east-west direction on the equatorial beta plane. *J. Meteor. Soc. Japan,* **69,** 595–608.